Hyperspectral and Multiangle CHRIS–PROBA Images for the Generation of Land Cover Maps

Riccardo Duca and Fabio Del Frate, *Member, IEEE*

***Abstract*—The small hyperspectral imager Compact High-Resolution Imaging Spectrometer (CHRIS) is the most important instrument for Earth observation included in the payload of the European Space Agency Third-Part Mission Project for On-Board Autonomy (PROBA)-1 satellite. This instrument has provided dozens of images in several target areas in the world, and a good number of acquisitions are available for the test site of Frascati and Tor Vergata, Italy. This paper reports several results concerning the generation of thematic maps obtained from CHRIS mode-3 imagery. The potential of the use of different configurations for the input vector exploiting multispectral, multiangular, and multitemporal measurements has been investigated, and the results have been evaluated and compared in terms of accuracy in the classification. The core of the decision task has been developed using the neural network methodology. Indeed, this approach is characterized by a particular ease in performing nonlinear mapping of a multidimensional set of inputs into the output one.**

***Index Terms*—Hyperspectral, land cover, neural networks, Project for On-Board Autonomy (PROBA)-1.**

I. Introduction

THE Project for On-Board Autonomy (PROBA)-1 satellite was launched in the 2001 with the principal aims of developing new technologies and solutions in platform design, space navigation, and orbit tracking and maintaining. The payload includes two instruments for Earth observation: the high-resolution camera and the Compact High-Resolution Imaging Spectrometer (CHRIS). CHRIS provides acquisitions up to 62 narrow and quasi-contiguous spectral bands with the spatial resolution of 34–40 m (mode 1), and it is also possible to plan observations with an increased resolution of 17–20 m using only a subset of 18 spectral bands. These spectral subsets or modes correspond to different band configurations providing data at an increased resolution for specific studies over land and water. Mode 2 provides images characterized by bands particularly tuned to observe water bodies and coastal phenomena, whereas modes 3 and 3a are recommended for land-use and land-change investigations. Mode 4 is used for chlorophyll content retrieval, and finally, mode 5 is an extended mode characterized by more than 18 bands (37) acquired only over half swath.

Manuscript received October 1, 2007; revised March 1, 2008. Current version published October 1, 2008. This work was supported by the European Space Agency under CAT-1 Project 3075.

The authors are with the Department of Computer Science, Systems and Production Engineering (DISP), University of Rome Tor Vergata, 00133 Rome, Italy (e-mail:duca@disp.uniroma2.it; delfrate@disp.uniroma2.it).

Color versions of one or more of the figures in this paper are available online at http://ieeexplore.ieee.org.

Digital Object Identifier 10.1109/TGRS.2008.2000741

From the scientific point of view, one of the most interesting capabilities of this satellite consists of tilting the spacecraft on two axes, along and across track, during the target overpass, allowing quasi-simultaneous acquisitions under five different angles. More particularly, the images are acquired when the zenith angle of the platform, with respect to the fly-by position, is one of the following: $+55^\circ$, $+36^\circ$, 0°, -36°, or -55°. The fly-by position is the point on the subsatellite track that is closest to the target site. This multiple-view-angle imaging capability, in addition to the high spectral and spatial sensor resolution, permits the collection of a large amount of data in order to perform new studies regarding the land and the atmosphere [1].

Other satellite missions have been providing information on the viewing direction and the directional anisotropy behavior of different surfaces. The multiangle imaging spectroradiometer (MISR) instrument on board NASA's Terra platform acquires reflectance data from any Earth target in four solar spectral bands, from nine different directions, in at the most 7 min, at a spatial resolution of 275 m in all bands of the nadir camera and in the red band of the off-nadir cameras and 1.1 km in the remainder [2], [3]. ADEOS–POLDER data are also an interesting example of multiangle exploitation in remote sensing, but because of their coarse spatial resolution, they are more suitable for monitoring atmospheric processes [4]. Higher spatial resolution multiangular data have been provided by airborne campaigns such as DAISEX [5] and AMTIS [6], which, however, are characterized by localized and temporally limited acquisitions. Therefore, the PROBA mission and the CHRIS property of joining both hyperspectral and directional sampling with high spatial resolution represent a new promising scenario for the generation of land cover products from remotely sensed data.

In this paper, only acquisitions in mode 3 have been considered. This configuration is characterized by 18 spectral bands covering the visible and the near-infrared range at 18 m of spatial resolution and, as already mentioned, is particularly suitable for land studies. Bands for atmospheric correction are present (442 and 490 nm), and also, the red edge range (between 700 and 800 nm) is well sampled in order to produce an accurate identification and monitoring of crops and green areas. A summary of the spectral characteristics of mode-3 acquisition is reported in Table I, whereas in Table II, the correspondence between the fly-by zenith angle (FZA) and real acquisition angles for our test site is reported.

The area between Frascati and Tor Vergata is in a test site for the PROBA-1 mission and is also the area considered for this study. This is a mainly flat area located in the southeast of Rome $(41^\circ 51' 26'' \text{ N}, 12^\circ 40' 26'' \text{ E})$, which presents an interesting

TABLE I
WAVELENGTHS VALUES FOR CHRIS–PROBA MODE-3 SPECTRAL CONFIGURATION

BAND	MIN (nm)	MAX (nm)	MID (nm)	WIDTH (nm)
L1	438	447	442	9
L2	486	495	490	9
L3	526	534	530	9
L4	546	556	551	10
L5	566	573	570	8
L6	627	636	631	9
L7	656	666	661	11
L8	666	677	672	11
L9	694	700	697	6
L10	700	706	703	6
L11	706	712	709	6
L12	738	745	742	7
L13	745	752	748	7
L14	773	788	781	15
L15	863	881	872	18
L16	891	900	895	10
L17	900	910	905	10
L18	1002	1035	1019	33

TABLE II
FZA AND ACTUAL ACQUISITION ANGLES (DEGREES) USED FOR THE CLASSIFICATION OF MULTIANGULAR MEASUREMENTS

FZA	ZENITH ANGLE (1^{st} date)	AZIMUTH ANGLE (1^{st} date)	ZENITH ANGLE (2^{nd} date)	AZIMUTH ANGLE (2^{nd} date)
0	19.53	315.1	3.75	204.52
36	32.02	341.3	31.02	11.39
-36	36.24	214.7	36.5	194.19
55	50.28	356.7	53.0	12.0
-55	53.06	207.7	56.39	193.76

heterogeneous landscape. Permanent crops such as vineyards, olive trees, and other fruit trees are mixed with agricultural areas characterized by a growth cycle, mainly cornfields, and uncultivated areas or pasture. Artificial land cover consists of residential urban areas, industrial and commercial units, and different kinds of road networks. In particular, two types of asphalted surfaces can be distinguished: 1) a dark one (lower reflectance values), corresponding to motorways and big routes, and 2) a bright one (higher reflectance values), which is more typical of secondary or urban streets and of big parking areas close to industrial and public structures.

As the first step, this paper proposes some solutions for the signal processing procedures that precede the classification task. These are dedicated to the correction of radiometric artifacts and to the estimation and elimination of atmospheric effects in the calculation of the top-of-canopy (TOC) reflectance values. A qualitative analysis of the capabilities of multiangular acquisitions in discriminating among different types of surfaces in terms of their signatures is then presented. Finally, the results regarding the production of final land cover maps using different combinations of inputs are reported and commented. The information content used as input to the classification algorithm has been progressively enhanced starting from simple multispectral measurements until considering, as the final step, the fusion of multispectral, multiangular, and multitemporal acquisitions, thus exploiting a very attractive opportunity given by PROBA.

The core of all classification steps has been realized by means of neural networks, which in the last years have demonstrated at the same time a particular ease on managing a large domain of inputs and an important effectiveness in performing the decision task for the classification of remotely sensed images [7].

II. PREPROCESSING STAGE

The CHRIS images are delivered at level 1A after the radiometric and spectral calibration. However, some artifacts are still present in the images, and for this reason, a further radiometric equalization is needed. The first fault characterizing the row data is represented by the presence of black pixels (pixels without useful information) with a periodic structure along the rows. This kind of artifact has been compensated by the use of a moving mean filter, which can identify the black pixel and substitute its value with the mean calculated over the window centered on the corrupted pixel. A second typical shortcoming due to the optical array detectors is the appearance in the images of stripes along the column direction. In order to tackle this noise, the methodology proposed by Settle [8] has been implemented and improved. This methodology is based on deleting the high-frequency components in the power spectrum by the use of a low-pass filter. In other words, the stripes produce high spatial variability among the columns, and this effect can be observed in the spatial frequency domain with the presence of components at high frequency [8]. These signals at high frequency can be deleted by applying a low-pass filter directly to the frequency spectrum or by applying a numeric smoothing filter to the image. Our efforts have been focused on the low-pass filtering methodology, which is implemented with a low-pass digital Butterworth filter applied on the fast Fourier transform of the column means [9]. The cleaned frequency spectrum is finally compared with the original one in order to calculate the coefficients for the final equalization. The last version of this algorithm has been integrated with a statistical module for automatic cloud masking. This allows excluding from the mean column value computation the reflectance values of saturated pixels inside clouds and snow. In Fig. 1, an example of the performance of the implemented destriping procedure is shown, considering band 1. In Fig. 2, the final destriped red–green–blue (RGB) image of the test site is reported.

The second important step of the preprocessing phase is with regard to the atmospheric correction. This step plays an important role in our applications, because the merging of images acquired under different angles of view and on different dates requires systematic compensation of the atmospheric effects, which are strictly dependent on the geometry of the acquisition and on the seasonal condition. The first issue consists of estimating the contribution of the atmospheric effects in terms of the total irradiance, the direct and diffuse transmittance, and the radiance due to the scattering. These parameters are related to the acquisition day (solar irradiance and position of the Earth with respect to the sun), to the atmospheric conditions (aerosol concentration and chemical profile of the atmosphere), and to the geometry of the acquisition (zenith angle of view and time of acquisition). The estimations have been produced starting from simulations carried out with the suite of libraries

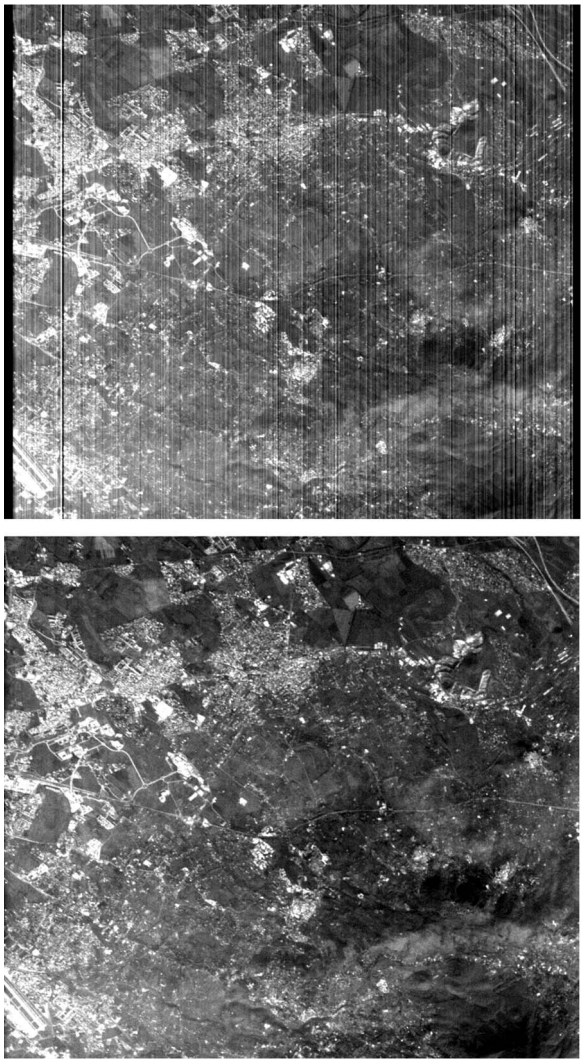

Fig. 1. Acquisition related to December 15, 2004, band 1. (Top) Before destriping. (Bottom) After destriping.

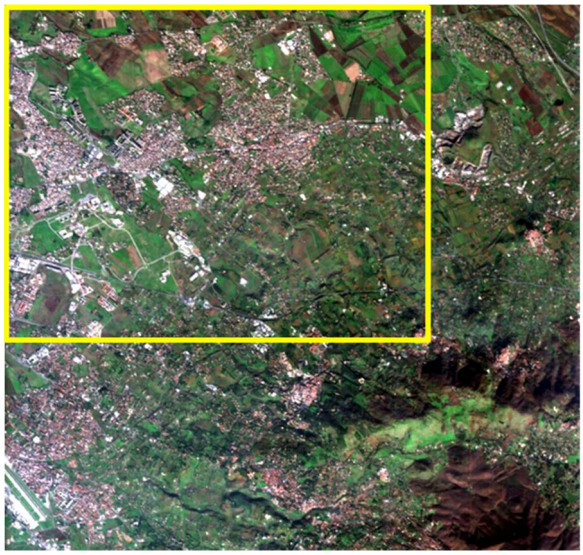

Fig. 2. CHRIS–PROBA RGB image of the test site after destriping and the area considered for the classification tasks.

libRadtran for the simulation of the radiative transfer balance [10]. In order to perform the simulations, standard seasonal profiles for the atmosphere have been considered, whereas the aerosol characterization, in terms of aerosol optical thickness and single scattering albedo, has been obtained by the integration with the measurements performed by the sun photometer at the Consiglio Nazionale delle Ricerche Tor Vergata and is available under the NASA Aerosol Robotic Network (http://aeronet.gsfc.nasa.gov) Project. The correction has been performed by implementing the following relation [11]:

$$\rho(\lambda,\theta) = \frac{\pi\left(L_{TOA}(\lambda,\theta) - L_{\text{path}}(\lambda,\theta)\right)}{E_0(\lambda,\zeta)T(\lambda,\theta)} \tag{1}$$

where $L_{TOA}(\lambda,\theta)$ is the radiance at the top of the atmosphere, $L_{\text{path}}(\lambda,\theta)$ is the radiance scattered by the atmosphere along the direction of the view, $E_0(\lambda,\xi)$ is the total irradiance at the top of the canopy, and $T(\lambda,\theta)$ is the total transmittance of the path from the target to the sensor. After the atmospheric calibration, the pixel adjacency correction has been also carried out by the use of weighted average in a large window applied to the whole image [11]

$$\rho^{(2)}(x,y) = \rho^{(1)}(x,y) + q\left\{\rho^{(1)} - \overline{\rho}(x,y)\right\} \tag{2}$$

$$\overline{\rho}(x,y) = \frac{1}{N^2}\sum_{i,j=1}^{N}\rho_{i,j}^{(1)}(x,y) \tag{3}$$

where $\rho^{(2)}(x,y)$ is the corrected radiance of a pixel, $\rho^{(1)}(x,y)$ is the original radiance of the pixel, q is the ratio between the diffuse and the direct transmittance, and $\overline{\rho}$ is the mean radiance calculated in a window of $N \times N$ pixels. The value 11 for N has been considered in this study and gave satisfactory results.

Once calibrated, the images had to be coregistered. The coregistration of all images, particularly those taken at different incidence angles, has been one of the most delicate steps and has been preliminary to the multiangular analysis and to the subsequent classification procedure. We considered as master the image taken with the larger acquisition angle, and before starting the coregistration, all other images have been resized to have the same spatial resolution. This led to having a pixel size of 23 m for all considered images, which softly degrades the spatial resolution of nadir images but allowed us to have good overlapping among different angle acquisitions.

Finally, the images have been georectified using a semiautomatic methodology based on the manual selection of ground control points and taking as master a very high resolution (VHR) pansharpened Quickbird image (0.63-m resolution) acquired over the same area in February 2002. On its turn, the master image has been previously rectified with several GPS ground control points. A final geometric precision of less than one pixel has been achieved, which can be recognized as satisfactory for this context.

III. Multiangular Analysis

Once the described preprocessing steps have been carried out, the image pixels represent the reflectance values calculated

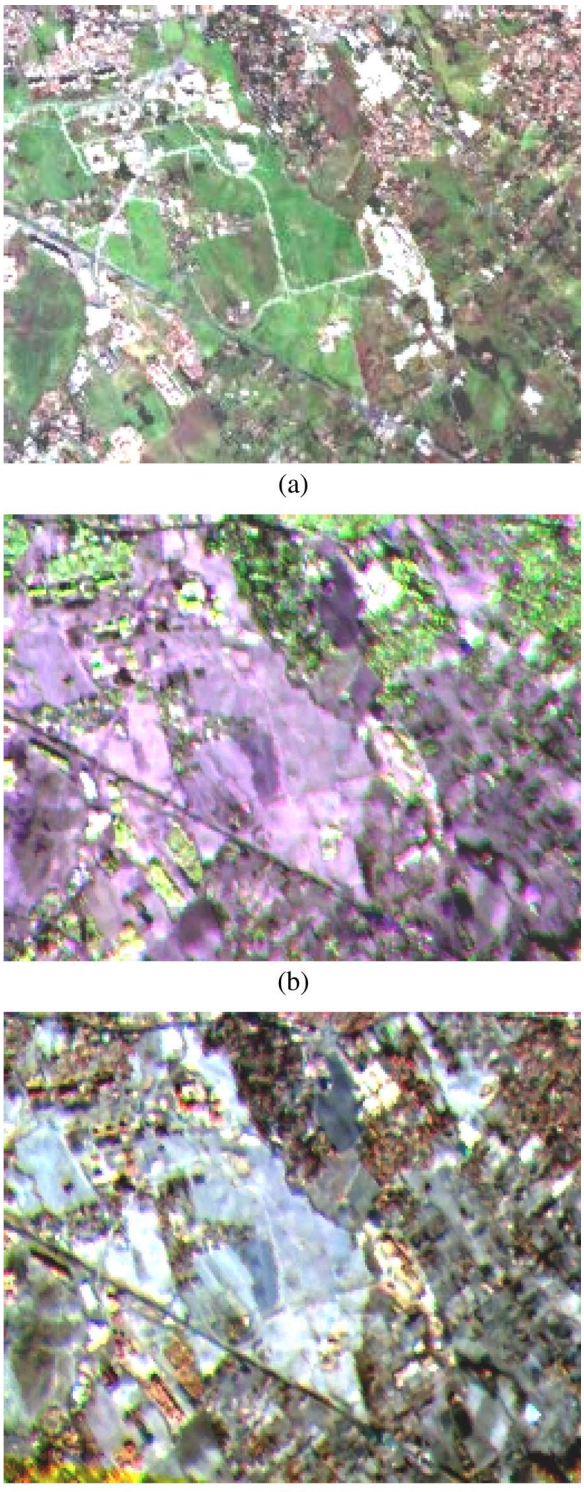

Fig. 3. (a) True color image composition. (b) Image composition using FZAs $-36°$, $0°$, and $36°$. (c) Image composition using FZAs $0°$, $36°$, and $55°$.

at the top of the canopy (TOC reflectance). In this section, the results stemming from a multispectral and multiangular reflectance analysis are reported and critically discussed for several surfaces.

The first investigation aims at discovering differences over natural and man-made surfaces in terms of multiangular acquisitions. The first example in Fig. 3 focuses on the area of

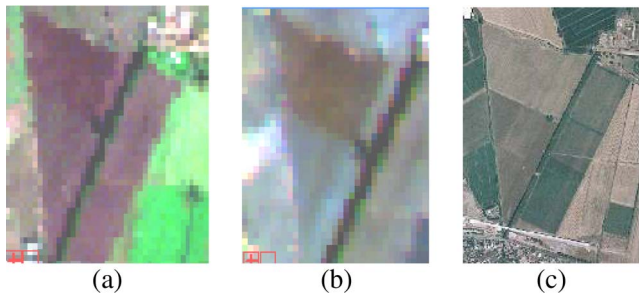

Fig. 4. (a) True color composition. (b) Multiangle composition using band 10 (703 nm). (c) VHR image.

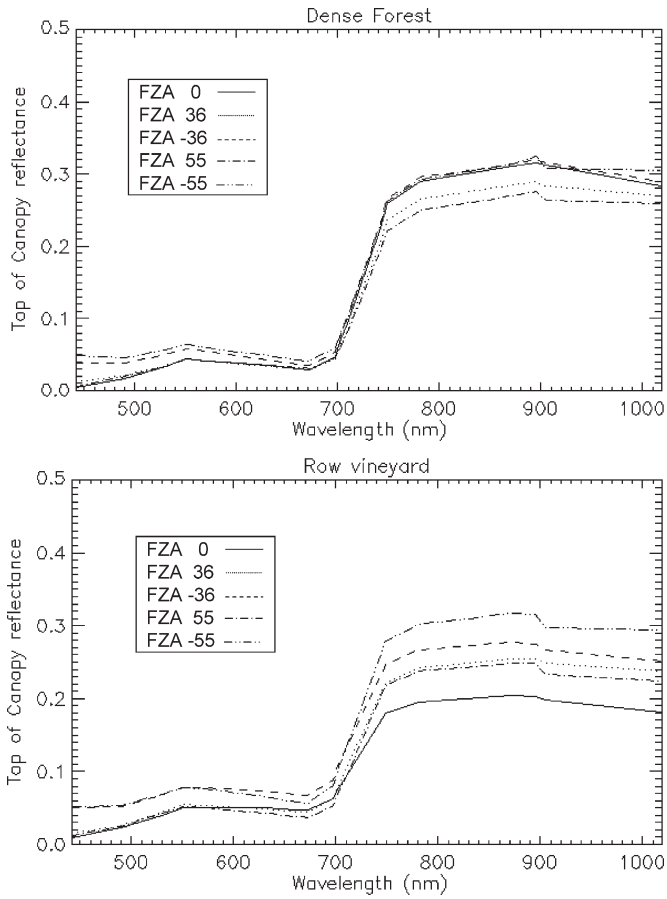

Fig. 5. Multiangle reflectance of permanent crops. Number of considered pixels: 50 for forest and 80 for vineyards.

the University of Rome Tor Vergata. In this case, two different multiangular compositions have been generated, considering band 10 (703 nm). We can note that some features can be better retrieved in the angular compositions in Fig. 3(b) and (c) with respect to the true color image in Fig. 3(a). For example, the multiangular compositions allow a clearer perception of differences in vegetation density. Areas of bare soil [dark areas in Fig. 3(b) and (c)] are more visible as well. The urban structures can be well discriminated using the compositions in Fig. 3(b) and (c), and it is possible to perform a preliminary distinction among different kinds of buildings. In fact, the residential buildings appear in a different color, green in Fig. 3(b) and red in Fig. 3(c), with respect to the brighter commercial and industrial buildings. Indeed, industrial and commercial blocks

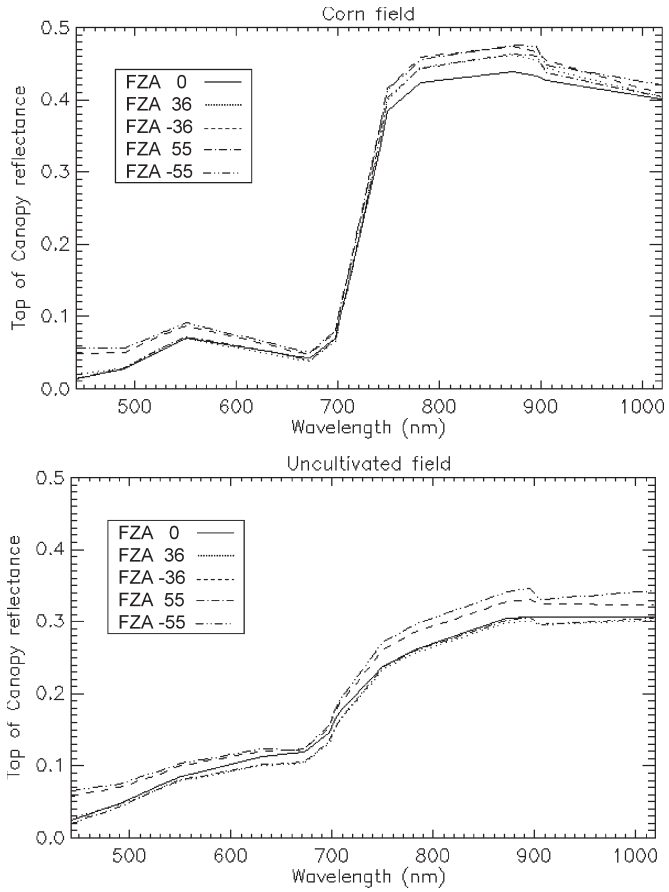

Fig. 6. Multiangle reflectance of vegetated areas. Number of considered pixels: 80 for corn and 50 for uncultivated areas.

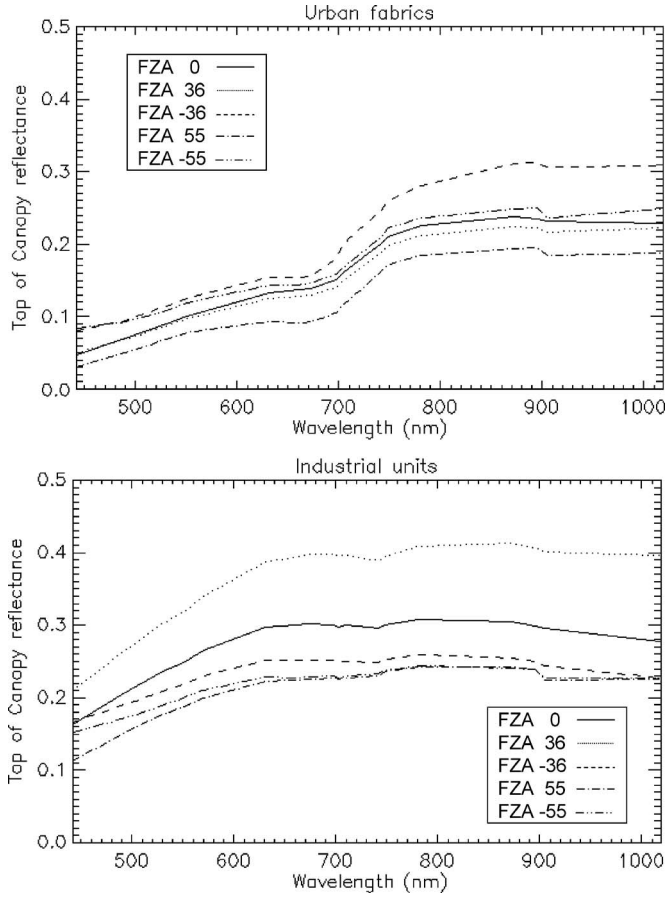

Fig. 7. Multiangle reflectance of built areas. Number of considered pixels: 100 for urban fabrics and 50 for industrial units.

are, in general, characterized by a less complex geometry and a smaller height with respect to residential buildings. This could yield different values of the reflectance in the multiangle acquisitions. A second example is proposed in Fig. 4, where some fields of maize have been observed. In this case, the multiangular composition in Fig. 4(b) reports two different responses for the reflectance values inside the big triangular field. This could be due to a different stage of cultivation or plant growth. The VHR image confirms that the field is really composed by two different areas. These differences are less evident in the RGB true color composition in Fig. 4(a).

After this preliminary visual analysis, several polygons, representing different typologies of land cover classes (vegetated areas, permanent crops, asphalted surfaces, and buildings), have been selected from the images and the angular signatures of the reflectances plotted. The polygons have been extracted from the inner part of the area of interest to minimize the effects of the surroundings. Moreover, all the spectra have passed the atmospheric calibration. The signatures of two types of permanent crops (Fig. 5), of two types of vegetated areas (Fig. 6), of two urban zones with different structures (Fig. 7), and of two types of asphalt coverages (Fig. 8) are reported. All five different angle acquisitions are considered and analyzed. Fig. 5 shows that the reflectance values calculated over row vineyards have greater sensitivity to the angle of acquisition than those of the dense forest. In fact, this crop is characterized by a particular geometric distribution of plants (along rows separated with a distance of 2 m), whereas for the forest, the distribution of canopies is homogeneous and very dense. For vegetated areas, a similar trend with angle variation is observed. Considering urban areas, both residential buildings and commercial/industrial units present a large sensitivity of reflectance with respect to the angle of acquisition. In particular, for commercial and industrial structures, we can see that rather high values in the spectral signature have been measured for the image related to the acquisition of FZA 36°. Results concerning asphalted surfaces are shown in Fig. 8. In both cases, the spectral signatures extracted from all multiangle images are rather close to each other. This confirms that the flatness characterizing such surfaces lowers the directional sensitivity of the reflectance. However, for shorter values of wavelengths, the bright asphalted surfaces (secondary roads and urban parking areas) exhibit some sensitivity to the acquisition angle. Conversely, for dark asphalt-covered surfaces (motorways and state highways), a significant dependence of the signature for the whole considered spectral range can be noted.

IV. Neural Network Classification

For the decision task, a pixel-based classification scheme based on neural networks has been developed [12]. The classification has been initially performed for both single-angle and multiangle acquisitions with the purpose of evaluating the

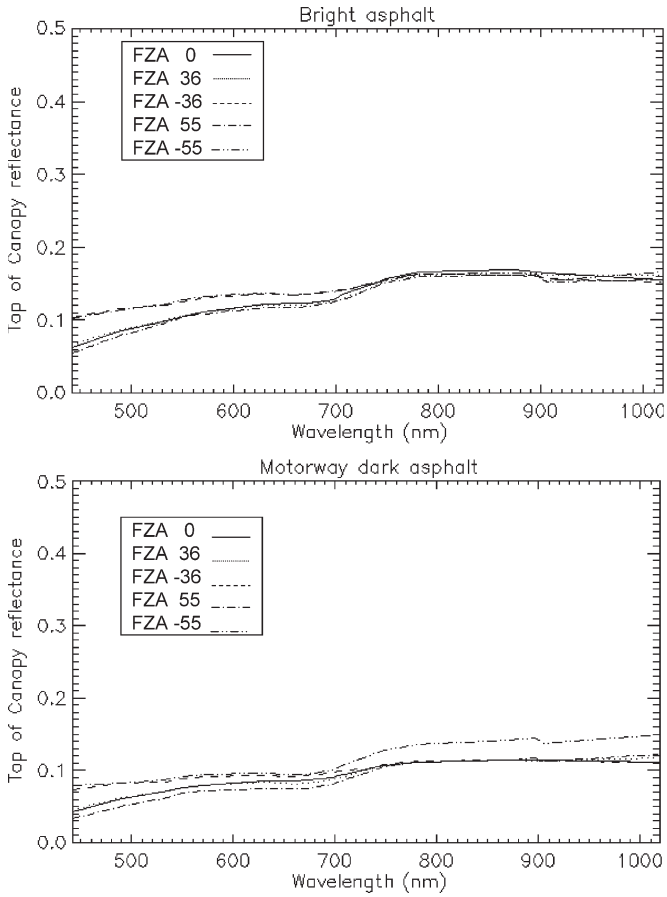

Fig. 8. Multiangle reflectance of different asphalted surfaces. Number of considered pixels: 30 for bright asphalt and 20 for dark asphalt.

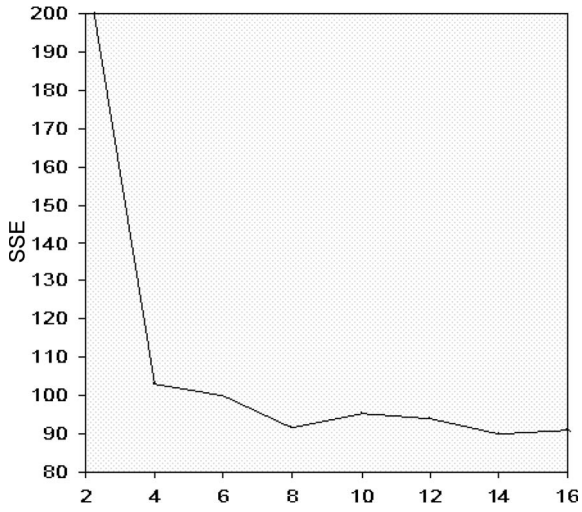

Fig. 9. SSE versus the number of hidden units for the neural network used in the multispectral classification. The horizontal axis indicates the number of units for each of the two hidden layers

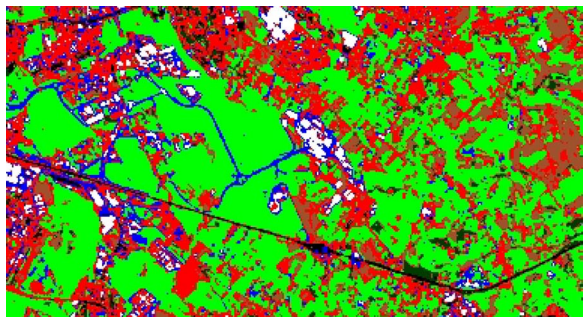

Fig. 10. Classified maps related to the nadir image of February 28, 2006. (Blue) Bright asphalt. (Black) Dark asphalt. (Green) Vegetated areas. (Dark green) Forest and permanent crops. (Red) Urban structures. (White) Industrial and commercial areas. (Brown) Bare soil.

improvement of the enhanced input vector in terms of accuracy and detail in the production of the thematic maps.

Regarding the network topology, the multilayer perceptron seems to be the best configuration for solving problems of classification and inversion [13] and has been considered for this study. The learning process has been carried out using two data sets: 1) a training set and 2) a validation set. The number of hidden layers and the amount of units composing each layer have been obtained after a systematic analysis. The best configuration is found when the minimum of the error function is reached on the test set. In our applications, the error function calculates the sum-of-square errors (SSEs), considering all patterns. In general, for the considered cases, the number of hidden layers has been two, whereas the number of hidden units changed according to the classification problem. The minimization of the error function has been pursued by a scaled conjugate gradient algorithm, which uses the second-order derivative of the error function [14]. The Stuttgart neural network simulator, made available by the University of Stuttgart, Stuttgart, Germany, has been used to design the network topology and perform the learning phase [15].

In the first classification exercise, the input vector feeding the network contained only the nadir measurements. More exactly, these results are related to the CHRIS observation on February 28, 2006 over the test site. At this stage, we identified some basic classes usually considered for the generation of land cover products from satellite high-resolution images, such as residential buildings, industrial and commercial units, bare natural soils, vegetated areas, and forest (including permanent crops). Water surfaces were not present in the area, but as a distinction between different asphalt coverages is, in principle, possible according to Section III, the dark asphalted and bright asphalted classes have been added to the more traditional ones. A total number of 915 and 896 pixels have been chosen for generating the sets with the training and the test patterns, respectively. The best topology obtained for the network is characterized by 18 inputs, two hidden layers of 14 units, and 7 units of outputs. The trend of SSE values versus the number of units in a two-hidden-layer topology is plotted in Fig. 9. The analogous analysis carried out with one hidden layer provided slightly worse results. Similar plots, not reported in the paper, have also been obtained for the successive neural network exercises. The classified map composed of almost 85 000 pixels and obtained with the selected topology is presented in Fig. 10, whereas the accuracy is reported in Table III. The accuracy has been calculated by selecting a significant number (5216) of ground-truth points validated on VHR Quickbird imagery and by direct inspections on the site. The confusion matrix reports an overall precision of 85.7%. The result is negatively conditioned by a rather coarse performance for the bright

TABLE III
CONFUSION MATRIX OBTAINED IN THE CLASSIFICATION OF THE NADIR IMAGE. THE REPORTED VALUES ARE IN PERCENTAGE. THE OVERALL ACCURACY IS OF 85.7% CONSIDERING 5216 POINTS OF GROUND TRUTH

	GROUND TRUTH						
	Dark Asphalt	Bright Asphalt	Urban Buildings	Industrial and Commercial units	Bare soil	Green vegetated areas	Forest and permanent crops
Dark Asphalt	85.4	4.6	1.0	0.0	0.2	0.0	0.0
Bright Asphalt	0.3	53.8	6.4	1.5	0.0	0.1	0.0
Urban Buildings	10.1	27.0	84.0	1.5	29.5	0.0	0.0
Industrial and commercial units	0.0	14.3	0.7	97.0	0.0	0.0	0.0
Bare soil	2.1	0.3	6.1	0.0	70.1	1.9	7.3
Green vegetated areas	0.0	0.0	1.8	0.0	0.1	98.0	9.1
Forest and permanent crops	2.1	0.0	0.0	0.0	0.1	0.0	83.6

asphalted surfaces. In fact, this feature in the images sometimes appears easily confused with the adjacent pixels, particularly when the acquisition is done under particular geometric configurations (large off-nadir angles). In Table III, we note that another source of error is the confusion between bare soil and residential buildings. This is a known problem in the classification of optical images characterized by high and very high spatial resolution and is due to resemblances in the spectra between the two surfaces.

In the second exercise, we generated the same land cover map, this time using multiangular images as inputs. Following what is shown in the multiangle analysis, the particular directional sensitivity of the reflectance of some surfaces produced a significant improvement compared to the results reported in Table III. The acquisition is again that on February 28, 2006 over the Frascati and Tor Vergata test site, but in this case, the images at FZAs 36° and −36° have been also considered together with the nadir image (FZA 0°) for the generation of the input vector. The same subimages as in the previous case have been extracted, and after the radiometric and atmospheric corrections, they have been coregistered and stacked in order to obtain a unique image composed of 54 spectral bands. The neural network has been learnt using the same training and validation data sets as the previous exercise, having in this case the best topology composed of 54 inputs, two hidden layers of 24 units, and the same seven classes of output. The land cover map is reported in Fig. 11. The accuracy is calculated using the same ground truth as the first classification, and Table IV shows the changes in terms of accuracy. We can see that for residential small buildings, bare soils, and asphalted surfaces, a significant increase in the accuracy values has been obtained thanks to the multiangular characterization. The overall improvement calculated for this scenario is around 7%. Considering the strong angular and directional dependence of the reflectance for industrial and commercial units, changes in accuracy could also be expected for this class, but after the classification, there is no evidence of improvements. This might have happened because deformations on buildings' shapes are present in the off-nadir views, and for this reason, an imperfect overlap of these structures could occur among the stacked images. The problematic coregistration of these pixels could have generated a noise that prevented us from obtaining the expected improvement for this class.

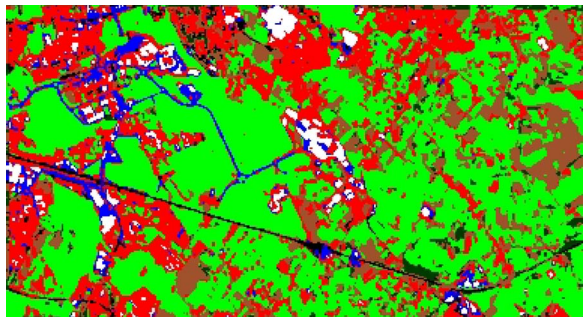

Fig. 11. Classified maps generated by the use of three multiangular images related to the acquisition on February 28, 2006. Color code is the same as Fig. 10.

TABLE IV
IMPROVEMENTS OBTAINED WITH THE USE OF THE MULTIANGLE ACQUISITION WITH RESPECT TO THE NADIR ACQUISITION. THE OVERALL ACCURACY IS 92.4%

SURFACE	IMPROVEMENTS
Dark Asphalt	-3%
Bright Asphalt	+27%
Urban buildings	+10%
Industrial/commercial units	Not relevant
Bare soil	+19%
Green vegetated areas	Not relevant
Forest and permanent crops	Not relevant

V. FURTHER POTENTIALITIES GIVEN BY MULTITEMPORAL DATA

The PROBA mission acquisition plan allows us to take more images during the same year over the same test site. This is another important characteristic of the mission, which therefore allows us to concurrently exploit hyperspectral, multiangular, and multitemporal information. To analyze what is the impact

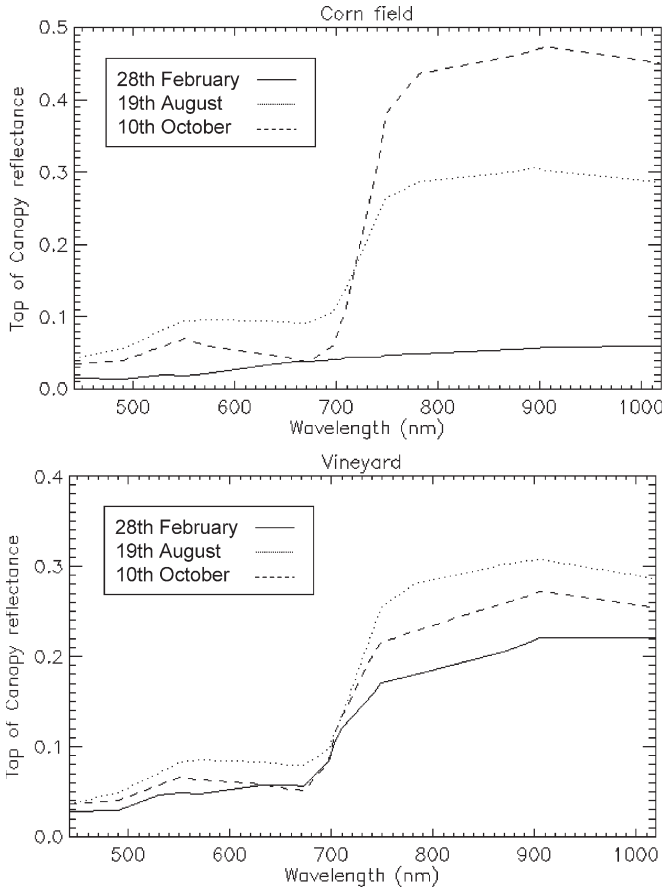

Fig. 12. Multispectral signatures of two different crops at three different dates.

of such capabilities in terms of final land cover products, we performed two final classification exercises. In the first one, the land cover map is obtained only with multitemporal and multispectral acquisitions; in the second one, the multiangular information is added, and as in Section IV, the improvements in terms of classification accuracy are evaluated. The attempt of considering at the same time multiangular and multitemporal acquisitions led to a redefinition of the area of interest, even if belonging to the same test site. This is due to different concurrent reasons such as small shifts affecting the images acquired at different times, shifts between images taken at different angles, sensitivity to clouds, and the need to limit the coregistration errors. Because of the same kind of constraints, we also had to restrict the multiangular information to two different angles (FZAs 0° and 36°). The multitemporal information is based on three images taken at the following dates: 1) February 28, 2006; 2) August 19, 2006; and 3) October 9, 2006. Such dates are, in principle, particularly suitable to sample the crops' growth cycle. In Fig. 12, we report two examples that show how cultivated areas such as cornfields or vineyards significantly change their spectra during the year. However, the vegetation development is peculiar for each particular crop type, provoking significant differences in the associated multitemporal signatures. Therefore, positive effects, particularly on crop discrimination, can be expected. With respect to the previous cases, the vineyards and cornfields, largely diffused in the selected area, have been extracted from the permanent-crop class and vegetated-area class, respectively, and have been considered as separate classes. We also treated uncultivated areas as a single class. In fact, their dependence with time should be rather different from that of cultivated fields. On the other hand, we eliminated the bare-soil class, as most of bare soils are cultivated fields at the very beginning of the growth cycle or after the harvest. In summary, we had to discriminate among nine classes with an input vector including 54 measurements (3×18). A new neural network algorithm has been trained using a training set and a test set of 3120 and 3045 patterns, respectively. A third different set of 21 766 ground-truth pixels has then been considered for the computation of the confusion matrix reported in Table V, whereas the classification and map is shown in Fig. 13. The same procedure has been applied to a new network that also has, as input, multiangular information. The acquisition at FZA 36° of the second date (month of August) was the additional piece of information. The choice of this date stems from the fact that the multiangular information should carry the best contribution when the agricultural fields are at the stage of full development. The corresponding results are reported in Table VI and Fig. 14. The validation on the ground truth demonstrates that both classifications have reported a high accuracy over all classes, always above 87% for any single class if we considered vineyards and other permanent crops as a unique class, with an overall improvement on the performance of more than 5% when the combined temporal and angular information is provided to the network. In particular, the most significant increase in the accuracy has been obtained for dark asphalted surfaces, uncultivated areas, and vineyards. The class of vineyard shows the best improvement, 11%, definitely mitigating the confusion with other permanent crops (olive groves and orchards). We do not have a better accuracy in all classes though. For the bright asphalt, it decreases by 2%, probably due to the errors introduced by a further step of coregistration.

VI. Conclusion

In this paper, we have investigated the potential of CHRIS–PROBA imagery to automatically produce maps of land cover. The design of optimum classifying schemes required the chaining of several processing steps. The first concerned the elimination of radiometric artifacts. Afterward, atmospheric effects had to be estimated using a radiative transfer model and, hence, removed. Up to 72 images have been successively coregistered to serve as input for the pixel-based classifier. Finally, a suitable neural network architecture had to be found to produce the maximum classification accuracy. In fact, the complete treatment of CHRIS imagery for "end-to-end" applications can be considered as the first significant result of the paper. The second aspect of the study deals with the new capabilities offered by the PROBA mission and CHRIS imagery in terms of information retrieval. The platform is conceived to monitor a region of interest at high spatial resolution with hyperspectral, multiangular, and multitemporal measurements. We have investigated how this may improve the discrimination among different land cover types. For example, the multiangle acquisition allows one to distinguish with appreciable accuracy (more than 80%) between dark asphalted (motorways) and bright asphalted (secondary roads and urban parking areas) areas. More generally,

TABLE V
CONFUSION MATRIX OBTAINED IN THE CLASSIFICATION OF THE NADIR IMAGE PLUS MULTITEMPORAL ACQUISITIONS (THREE DATES). THE REPORTED VALUES ARE IN PERCENTAGE. THE OVERALL ACCURACY IS OF 87.7% CONSIDERING 21 766 PIXELS OF GROUND TRUTH

	GROUND-TRUTH								
	Dark Asphalt	Bright asphalt	Urban Buildings	Industrial and Commercial Units	Uncultivated	Other permanent crops	Vineyards	Corn	Other agricultural areas
Dark Asphalt	88.8	1.4	0	0.4	0	0	0.1	0	0
Bright Asphalt	1.4	93	0.9	0.7	0.2	0	0	0	0
Urban Buildings	4.9	4	96.2	4.2	0.3	0	2.3	0.2	4.8
Industrial and Commercial Units	0	1.4	2.2	94.7	0	0	0	2.0	0
Uncultivated	4.9	0.2	0.4	0	86.4	1.7	5.1	0.1	0
Other permanent crops	0	0	0.1	0	3.3	83	15.7	0	0
Vineyards	0	0	0.2	0	5.7	14.1	73.0	2.6	0.6
Corn	0	0	0	0	3.6	0.2	3.5	95.1	0.1
Other agricultural areas	0	0	0	0	0.5	1.0	0.3	0	94.5

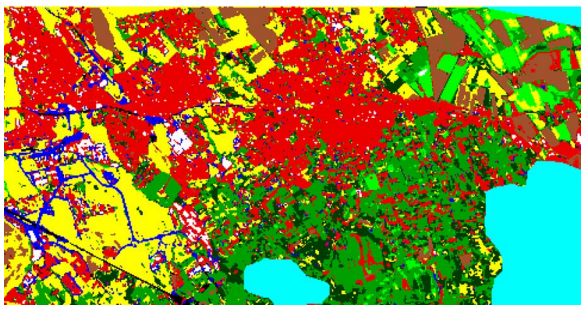

Fig. 13. Classified maps generated by the use of three multitemporal acquisitions: February 28, 2006, August 19, 2006, and October 9, 2006. (Blue) Bright asphalt. (Black) Dark asphalt. (Red) Urban structures. (White) Industrial and commercial areas. (Green) Vineyards. (Dark green) Other permanent crops. (Light green) Corn. (Brown) Other agricultural areas. (Yellow) Uncultivated. (Cyan) Masked areas (clouds and shadows).

TABLE VI
IMPROVEMENTS OBTAINED WITH THE USE OF THE MULTIANGLE ACQUISITION AND MULTITEMPORAL ACQUISITION WITH RESPECT TO THE MULTITEMPORAL ACQUISITION. THE OVERALL ACCURACY IS 92.9%

SURFACE	IMPROVEMENTS
Dark Asphalt	+6%
Bright Asphalt	-2%
Urban Buildings	Not relevant
Industrial/commercial units	Not relevant
Uncultivated	+8%
Other permanent crops	+1%
Vineyards	+11%
Corn	+2%
Other agricultural areas	+4%

the inclusion in the input vector of the spectra corresponding to three angular acquisitions (namely, at FZAs $-36°$, $0°$, and $+36°$) brings the overall classification accuracy to more than 92%, an improvement of almost 7% with respect to a single nadir acquisition. We have also seen that a further increase of the classification quality may be derived from the consideration in the processing scheme of the multitemporal measurements. We observed that the information brought in by multitemporal

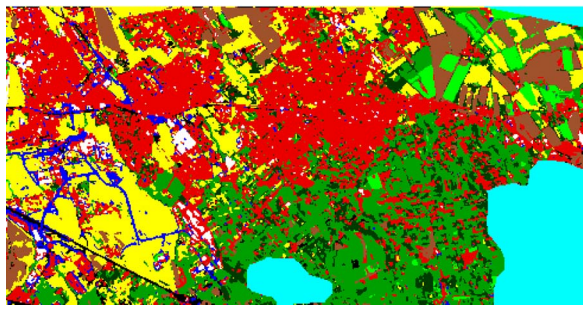

Fig. 14. Classified maps generated by the use of three multitemporal acquisitions—February 28, 2006, August 19, 2006, and October 9, 2006—plus the acquisition on August 19, 2006 taken at FZAs $0°$ and $36°$. Color code is the same as Fig. 13.

data, in addition to refining the classification in terms of discrimination levels, can also improve the accuracy rates, leading to overall accuracies of about 93%, considering nine different classes. We conclude by observing that future studies regarding PROBA imagery should be dedicated to developing techniques able to (automatically) manage the many available inputs with respect to the specific retrieval or classification problem at hand. Once again, our study demonstrates the effectiveness of neural network algorithms in positively combining different levels of information, but in particular, when more multitemporal acquisitions will be available during one year and over the same test site, we may easily reach hundreds of components for the input vector of the classification algorithm. At this point, a selection of the inputs to the network will be unavoidable to eliminate unnecessary or misleading quantities.

ACKNOWLEDGMENT

The authors would like to thank the student Carlo Brunamonti for carrying out the analysis leading to the best network topologies. The authors would also like to thank Prof. Solimini of the University of Rome Tor Vergata, Rome, Italy, and the anonymous reviewers for their useful suggestions and criticisms.

REFERENCES

[1] M. J. Barnsley, J. J. Settle, M. A. Cutter, D. R. Lobb, and F. Teston, "The PROBA/CHRIS mission: A low-cost smallsat for hyperspectral multiangle observations of the Earth surface and atmosphere," *IEEE Trans. Geosci. Remote Sens.*, vol. 42, no. 7, pp. 1512–1520, Jul. 2004.

[2] D. J. Diner, J. C. Beckert, T. H. Reilly, C. J. Bruegge, J. E. Conel, R. A. Kahn, J. V. Martonchik, T. P. Ackerman, R. Davies, S. A. W. Gerstl, H. R. Gordon, J.-P. Muller, R. B. Myneni, P. J. Sellers, B. Pinty, and M. M. Verstraete, "Multi-angle imaging SpectroRadiometer (MISR) instrument description and experiment overview," *IEEE Trans. Geosci. Remote Sens.*, vol. 36, no. 4, pp. 1072–1087, Jul. 1998.

[3] V. N. Sridhar, R. R. Navalgund, and A. Mahtab, "Impact of surface anisotropy on classification accuracy of selected vegetation classes: An evaluation using multidate multiangular MISR data over parts of Madhya Pradesh, India," *IEEE Trans. Geosci. Remote Sens.*, vol. 46, no. 1, pp. 250–258, Jan. 2008.

[4] S. Mukai and I. Sano, "Retrieval algorithm for atmospheric aerosols based on multi-angle viewing of ADEOS/POLDER," *Earth Planets Space*, vol. 51, no. 11, pp. 1247–1254, 1999.

[5] M. Berger, M. Rast, P. Wursteisen, E. Attema, J. Moreno, A. Müller, U. Beisl, R. Richter, M. Schaepman, G. Strub, M. P. Stoll, F. Nerry, and M. Leroy, "The DAISEX campaigns in support of a future land-surface-processes mission," *ESA Bull.*, no. 105, pp. 101–111, Feb. 2001.

[6] W. Huang, Z. Niu, J. Wang, L. Liu, C. Zhao, and Q. Liu, "Identifying crop leaf angle distribution based on two-temporal and bidirectional canopy reflectance," *IEEE Trans. Geosci. Remote Sens.*, vol. 44, no. 12, pp. 3601–3609, Dec. 2006.

[7] F. Del Frate, F. Pacifici, G. Schiavon, and C. Solimini, "Use of neural networks for automatic classification from high-resolution images," *IEEE Trans. Geosci. Remote Sens.*, vol. 45, no. 4, pp. 800–809, Apr. 2007.

[8] J. C. Garcia and J. Moreno, "Removal of noise in CHRIS/Proba images: Application to the SPARC campaign data," in *Proc. 2nd Chris Proba Workshop*, Apr. 28–30, 2004, [CD-ROM].

[9] S. K. Mitra, *Digital Signal Processing, A Computer-Based Approach*, 2nd ed. New York: McGraw-Hill, 2001.

[10] B. Mayer and A. Kylling, "Technical note: The libRadtran software package for radiative transfer calculations—Description and example of use," *Atmos. Chem. Phys.*, vol. 5, no. 7, pp. 1855–1877, 2005.

[11] E. Vermote, N. El Saleous, C. Justice, Y. Kaufman, J. Privette, L. Remer, J. Roger, and D. Tanré, "Atmospheric correction of visible to middle-infrared EOS-MODIS data over land surfaces: Background, operational algorithm and validation," *J. Geophys. Res.*, vol. 102, no. D14, pp. 17 131–17 141, 1997.

[12] C. Bishop, *Neural Networks for Pattern Recognition*. New York: Oxford Univ. Press, 1995.

[13] S. Y. Hsu, T. Masters, M. Olson, M. Tenorio, and T. Grogan, "Comparative analysis of five neural network models," *Remote Sens. Rev.*, vol. 6, no. 1, pp. 319–329, 1992.

[14] M. Møller, "A scaled conjugate gradient algorithm for fast supervised learning," *Neural Netw.*, vol. 6, no. 4, pp. 525–533, 1993.

[15] A. Zell *et al.*, "SNNS Stuttgart Neural Network Simulator User Manual," Univ. Stuttgart, Inst. Parallel Distrib. High Perform. Syst., Stuttgart, Germany, Tech. Rep. N.6/95, 1995. [Online]. Available: www.ra.informatik.uni-tuebingen.de/SNNS

Riccardo Duca received the Laurea (B.S.) and Laurea Specialistica (M.S.) degrees in telecommunication engineering from the University of Rome Tor Vergata, Rome, Italy, in 2002 and 2004, respectively. He is currently working toward the Ph.D. degree in geoinformation in the Department of Computer Science, Systems and Production Engineering (DISP), University of Rome Tor Vergata.

From October 2006 until May 2007, he worked in the Department of Technology-Wave Interaction and Propagation Section (TEC-EEP), European Space Agency (ESA) European Space Research and Technology Centre, Nortwijk, The Netherlands, contributing to the preparation of the future multispectral mission Sentinel-2. He is currently a Visiting Scientist with the ESA Centre for Earth Observation (ESRIN), Frascati, Italy. During his career, he has been also involved in many other projects regarding the processing and the exploitation of microwave and optical remotely sensed data and their integration in geographic information systems. His main research activity is the processing and the use of multispectral and hyperspectral high-resolution imagery for target and surface identification. In particular, most of his work has been addressed toward the evaluation of space and airborne hyperspectral technology for the generation of land cover maps and for the simulation of future multispectral instruments.

Fabio Del Frate (M'03) received the Laurea degree in electronic engineering and the Ph.D. degree in computer science from the University of Rome Tor Vergata, Rome, Italy, in 1992 and 1997, respectively.

From September 1995 to June 1996, he was a Visiting Scientist with the Research Laboratory of Electronics, Massachusetts Institute of Technology, Cambridge. In 1998 and 1999, he was with the European Space Agency (ESA) Centre for Earth Observation (ESRIN), Frascati, Italy, as a Research Fellow and was engaged in projects concerning end-to-end remote sensing applications. Currently, he is a Research Professor with the Department of Computer Science, Systems and Production Engineering (DISP), University of Rome Tor Vergata, where he teaches courses in electromagnetics and neural networks. He has acted and is the Principal Investigator in several remote sensing projects supported by ESA. He is the author or a coauthor of more than 100 scientific publications, with a special focus on the applications of neural networks to remote sensing inversion problems. His main research topics include retrieval and classification algorithms for land cover from satellite data, oil spill detection in SAR imagery, retrieval of atmospheric variables with microwave radiometry, data exploitation for the new missions PROBA and OMI. He serves as a Reviewer for different remote sensing journals.

Dr. Del Frate is an Associate Editor for the IEEE GEOSCIENCE AND REMOTE SENSING LETTERS.